

# Guest-directed synthesis reveals vast family of robust polyphenolic metal-organic frameworks

Erik Svensson Grape<sup>1\*,§,#</sup>, Alfredo López-Olvera<sup>1,2,#</sup>, Yan Zheng<sup>1</sup>, Yu Xia<sup>1</sup>, Tom Willhammar<sup>1\*</sup>, A. Ken Inge<sup>1,2\*</sup>

Structure directing agents (SDAs) are widely used in the synthesis of ubiquitous porous materials, such as zeolites, but their application and role in the synthesis of metal-organic frameworks (MOFs) has been comparatively understudied. Here we report a diverse family of anionic MOFs with all frameworks constructed exclusively from the same metal cation and plant-based organic linker—Zr(IV) cations and ellagate anions. Applying the same synthesis conditions but only changing the species of the SDA resulted in 10 novel zirconium ellagate MOFs (denoted SU-103 – SU-112) with varying dimensionality, topologies, Zr(IV) coordination geometries, intermolecular framework interactions, and framework interpenetration. Modern electron diffraction and electron microscopy techniques revealed the location of the SDA molecules in the pores of all MOFs, enabling a detailed study of their interactions. Despite having similar framework compositions, the properties of these MOFs noticeably differ due to the different ammonium SDAs and the unique framework structures obtained. The MOFs demonstrate chemical stability in aqueous media, basic conditions, and concentrated salt solutions, which is attributed to the strong Zr-catecholate chelating interactions consolidating the frameworks. We anticipate these 10 MOFs are only a small portion of a potential plethora of MOFs that could be discovered within this system. This lays the groundwork for the discovery of many other chemically robust structure-directed MOFs made with different cationic SDAs, framework metal cations, as well as other organic linkers with polyanionic functional groups.

Porous materials are a diverse class of materials with widespread applications, and their properties are fundamentally dependent on the nature of their porosities. As such, controlling the dimensionality, size, shape, and composition of their pores is an essential part of developing materials for specific applications. Structure directing agents (SDAs) can be added during synthesis, which interact with the framework-forming species and direct the formation of a specific porous phase that would not form in their absence. The use of SDAs to develop novel porous materials is an attractive strategy as it allows for the formation of numerous porous framework architectures with the same framework composition. As the structure of the framework largely dictates its physical and chemical properties, the use of SDAs is important for developing a library of materials with differing properties. Once a framework structure (host) has formed, the SDAs will typically reside in the pores as guest species. As long as the framework is robust, SDAs may be post-synthetically removed or, in the case of ionic SDAs, exchanged for other ions.

The introduction of organic structure directing agents (OSDAs) by Richard Barrer was a pivotal development that propelled the expansion of synthetic zeolite structures.<sup>1</sup> In zeolite science, alkylammonium cations are perhaps the most widely used OSDAs, although phosphonium cations<sup>2</sup> and cationic metal complexes with alkylamine ligands have also been used in the development of novel phases.

Metal-organic frameworks (MOFs) are another class of porous materials and as the name suggests they are made of two main components that typically self-assemble in the absence of SDAs. In most cases the positive charge of the metal cation will be balanced by the negative charges of coordinating ligands such as the linker, bridging oxides/hydroxides, or terminal ligands such as OH<sup>-</sup> or F<sup>-</sup>. Therefore, the majority of MOFs are charge neutral. However, some MOFs have anionic or cationic frameworks, and require the presence of charge-balancing guest species in the pores. However, realizing that a MOF is ionic is not always trivial, especially by X-ray diffraction alone, and often requires additional characterization to investigate the (de)protonation of ligands and confirming the presence of charge balancing guest species in the pores, which may even be disordered. Considering this, we suspect that many reported MOFs may unknowingly be ionic.

The use of amines as OSDAs to direct the formation of anionic MOFs with different structures has been reported by a number of research groups<sup>3–8</sup>. However, it is only in very few cases that full ion exchange has been demonstrated as well as microporosity by gas sorption experiments<sup>9</sup>. This may be due in part to the SDAs often being trapped in the pores or inadequate robustness of the framework upon ion exchange resulting in collapse of the open framework.

Therefore, as for any material, suitable chemical robustness is vital for various applications, including for example aqueous stability for environmental remediation or thermal stability for high-temperature separations. One approach to promote

<sup>1</sup>Department of Materials and Environmental Chemistry, Stockholm University, Stockholm, 106 91, Sweden.

<sup>2</sup>Wallenberg Initiative Materials Science for Sustainability, Department of Materials and Environmental Chemistry, Stockholm University, Stockholm 106 91, Sweden.

<sup>§</sup>Current address: Department of Chemistry and Biochemistry, Materials Science Institute, University of Oregon, Eugene, OR 97403, United States

<sup>#</sup>These authors contributed equally to this work.

\*Corresponding authors. email: erik.svensson-grape@kemi.uu.se, tom.willhammar@mmk.su.se, andrew.inge@mmk.su.se

chemical robustness is the use of tri- or tetravalent metal cations combined with strongly chelating hard ligands in the design of MOFs.<sup>10,11</sup> Notably, a small number Zr(IV)-phenolate MOFs have been reported with very high chemical stability, in many cases with better stability compared to Zr-MOFs of similar pore size made from carboxylate linkers<sup>12–15</sup>. This trend in higher stability might in part be attributed to the stronger electrostatic interactions between Zr(IV) and the polyanionic catecholate group as well as a larger bite angle when compared to monoanionic carboxylates.

This has intrigued our interest in developing MOFs utilizing common polyphenolic natural products as organic linkers, especially those lacking carboxylate groups but having catecholate or pyrogallate groups that can strongly chelate metal cations to form robust MOFs. We have particularly focused on ellagic acid (EA). Ellagic acid is a centrosymmetric and planar molecule with two catechol functional groups on opposite ends. It is also rather inexpensive, making it an appealing MOF linker. Notably, this eco- and bio-compatible molecule is part of the natural human diet—found in fruits, nuts and berries—and is well known as an antioxidant. Ellagic acid is also the base unit of the class of naturally occurring polyphenols known as ellagitannins. While reagent-grade ellagic acid can be acquired from chemical suppliers, it is also sold as a dietary supplement. Independent of the supplier, it is typically sourced and extracted from plant-based materials, such as tree bark or fruit peels, which are waste materials from the food, pulp and paper industries.

We recently reported the first two MOFs made from ellagic acid, including a bismuth ellagate (SU-101)<sup>16</sup> and a zirconium ellagate (SU-102)<sup>17</sup> both exhibiting high chemical stability and microporosity. Since then, crystal structures of a calcium ellagate<sup>18</sup> and nickel ellagate<sup>19</sup> have also been reported by other research groups as well as ellagate-based COFs<sup>20,21</sup>. The original reported synthesis of SU-102, (DMA)<sub>2</sub>[Zr(EA)<sub>2</sub>], involved the use of a solvent mixture containing water, acetic acid and dimethylformamide (DMF). Of great importance to this work, DMF decomposes to form dimethylammonium (DMA) cations in the presence of water, which reside in the pores of the anionic SU-102 framework. Notably, DMF could be replaced as a reagent by other amines such as ammonia, dimethylamine, and diethylformamide, which *in situ* convert into ammonium, dimethylammonium, and diethylammonium cations respectively, all of which direct the formation of SU-102. The ammonium OSDAs can post-synthetically be exchanged for metal cations such as Li<sup>+</sup>, Na<sup>+</sup>, K<sup>+</sup> to tune the physical properties of the MOF such as accessible pore volume, surface area and selectivity in gas adsorption. However, these ammonium species used as OSDAs for SU-102 are all rather small OSDAs, comprising no more than five non-hydrogen atoms.

To comprehend the physical and chemical properties of porous materials and establish relationships between synthesis, structure and properties, a detailed understanding of the crystalline framework structures is vital. Recent developments of electron crystallography techniques, such as three-dimensional electron diffraction (3D ED) and aberration-corrected scanning transmission electron microscopy (STEM), have greatly facilitated structure elucidation. Three-dimensional electron diffraction (3D ED) is a technique that allows the acquirement of single-crystal diffraction data from submicrometer-sized crystals<sup>22–24</sup>. Through 3D ED measurements, the requirement of synthesis optimization to grow large crystals, which is typically required for structure determination by single-crystal X-ray diffraction, can be circumvented, also significantly accelerating materials discovery. Automation in electron diffraction is now further accelerating materials discovery<sup>25</sup>. Guest species have been located in the pores of nanoporous materials such as MOFs<sup>26</sup> and germanium oxides<sup>27</sup> using 3D ED. STEM imaging has evolved into an essential technique for atomic-scale local structural investigations especially important for materials with structural disorders and low-dimensional materials. In combination with 3D ED, it represents a comprehensive toolbox for the characterization of both average and local structure, exemplified by the structure elucidation of bismuth subsalicylate<sup>28</sup> and the discovery of the zeolitic nanotube<sup>29</sup>.

Here we present a family of 10 novel zirconium ellagate frameworks (SU-103 – SU-112) made from identical synthesis conditions with the exception that a different amine or ammonium reagent was used as the OSDA for each MOF, i.e. the same ratio of reagents, heating time and temperature have been applied. The convenience of being able to repeatedly apply similar and synthesis conditions and to determine the structures of these submicrometer-sized crystals quickly by 3D ED allowed for accelerated discovery of novel materials. The discovery of the guest-directed MOFs and the details of the interactions between framework and guest were made possible using electron crystallography and the systematic study of their location and coordination provide insight to the structure-directing role of the amines.

### Synthesis of zirconium ellagate frameworks (SU-103 – SU-112)

All novel zirconium-ellagate frameworks (SU-103 – SU-112) were synthesized from a mixture of 32 mg zirconyl chloride octahydrate, 60 mg ellagic acid, 2.5 mL water, 1.0 mL acetic acid and 1 mL / 1 g of an OSDA. Each mixture was heated for 1 h at 160 °C. The OSDA used for each MOF is presented in Fig. 1 and in Supplementary Fig. 1. Crystallinity was confirmed by powder X-ray diffraction (PXRD, Supplementary Fig. 22). To demonstrate the rapid development of MOFs combined with fast 3D ED structure determination, SU-106 was synthesized and its structure was solved in a single day (5 h 40 min). Synthesis was completed within 3 h 30 min, including lab preparation and measuring reagents (1 h 15 min), heating the reaction (1 h), washing and drying the product (1 h 10 min). PXRD was then performed within 50 min. TEM sample preparation took 35 min, and finally 3D ED data collection, processing and structure solution was complete in 50 min.



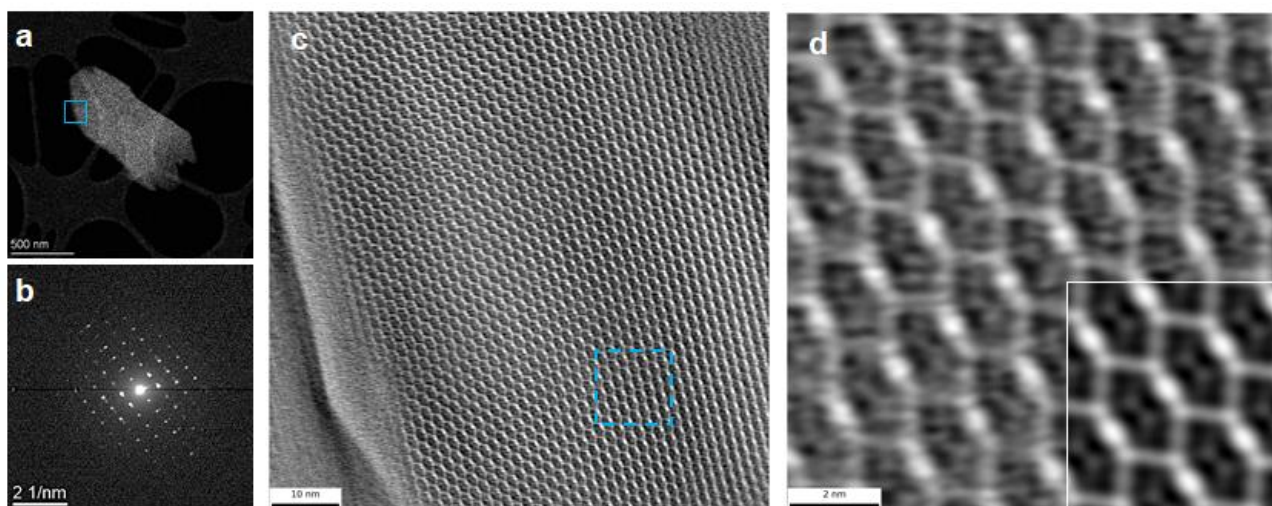


**Figure 2 | High-resolution STEM image of SU-107.** **a**, HAADF image of a thin flake of a SU-107 crystal. The blue square denotes the region imaged at higher magnification in (c). **b**, Corresponding selected area electron diffraction pattern obtained from the crystal in (a), which the lattice spacings measured from this diffraction pattern indicate the orientation is in the [100] direction. **c**, Reconstructed OBF-STEM image of the crystal, which was acquired with a dose rate of  $57 \text{ e}/\text{\AA}^2$ , showing a large hexagonal arrangement of pores. **d**, Enlarged OBF-STEM image of the area marked in (c) with the lattice averaged map in the plane group  $p2$  shown in the inset, providing a clear view of the well-ordered porous structure of SU-107.

Four of the MOFs exhibit a porous layered structure with the **hcb** net (SU-104, SU-108, SU-110 and SU-111), specifically forming 2D porous hexagonal honeycomb networks. In these structures, four ellagate ligands coordinate to each Zr(IV), three of them chelating through both oxygen atoms of the catecholate group, while the fourth ellagate ligand coordinates only through one phenolic oxygen atom resulting in a coordination number of seven for the Zr(IV) cations ( $\text{ZrO}_7$ ). There are also  $\pi$ - $\pi$  stacking interactions between ellagate anions which further stabilize the structures. In SU-104, SU-108 and SU-110, pairs of  $\pi$ - $\pi$  stacked ellagate linkers bridge the same two Zr(IV) nodes, forming a double ellagate bridge (Supplementary Fig. 13), yielding three-connected Zr(IV) nodes. In SU-111 on the other hand, one of the ellagate ligands is terminally coordinating while the remaining ellagate ligands singly bridge to three Zr(IV). This results in a notably different honeycomb network in which the terminally coordinating ellagate ligands are perpendicular to the layer, protruding out and  $\pi$ - $\pi$  stacking with ellagates from neighbouring layers.

The remaining six synthesized MOFs exhibit 3D framework structures with three distinct topologies (**nbo**, **dia**, **pcu**). Notably, SU-103 is the only structure in which pairs of Zr(IV) cations share two oxygen atoms, resulting in a dimeric  $\text{Zr}_2\text{O}_{12}$  inorganic building unit (IBU) that is connected to six other nodes in a cubic arrangement, forming a primitive cubic net, **pcu** (Supplementary Fig. 13). The previously described SU-102 material exhibits a **nbo** topology, in which Zr(IV) cations are eight-coordinated and all ligands participate in  $\pi$ - $\pi$  stacking interactions, which significantly contribute to the stability and structural integrity of the network. The most common topology among the synthesized MOFs is the **dia** net, as observed for SU-105, SU-106, SU-107, SU-109 and SU-112. In these structures, each Zr(IV) node is coordinated by four ellagate ligands in a tetrahedral arrangement to form 3D diamond nets. Among the five frameworks, the Zr(IV) cations in SU-107 and SU-109 are seven-coordinated, while eight-coordinated Zr(IV) nodes are present in SU-105, SU-106 and SU-112 (Supplementary Fig. 13). SU-107 possesses the largest pores of the 3D frameworks, and its crystals are well ordered as observed by optimum bright field scanning transmission electron microscopy (OBF-STEM) imaging, as shown in Fig. 2. Two of the six walls around each hexagonal pore have higher contrast since those walls have twice the density of ellagate linkers compared to the other four walls. SU-106 and SU-112 exhibit interpenetrated structures both comprising of the same individual frameworks. However, in SU-106, the two interpenetrated frameworks are related by translational symmetry, whereas in SU-112 the same two interpenetrated frameworks are not only translated with respect to one another but also rotated  $90^\circ$ . Therefore, in SU-106 the planar ellagate linkers are all aligned parallel to the channel direction, which contrasts with SU-112 where one of the frameworks has ellagates aligned perpendicular to the channels. Thus, these two phases are not interchangeable.

### Zr(EA)<sub>4</sub> isomers

Although several of the synthesized MOFs have the same framework topology—SU-104, SU-108, SU-110 and SU-111 all being described by the **hcb** net, or SU-105, SU-106, SU-107, SU-109, and SU-112 all with the **dia** net—it should be

**Table 1 | Distinguishing structural features of Zr-ellagate MOFs SU-102 – SU-112 and a summary of MOF-OSDA interactions.**

	dim.	net	space group	Zr(IV) C.N.	Zr <sub>x</sub> O <sub>y</sub>	ZrEA <sub>4</sub> isomer	Term. EA	EA π-π	unique amines	host-guest interactions	H-bonding oxygen*
<b>SU-110</b>	2D	hcb	<i>P</i> -1	7	ZrO <sub>7</sub>	2bbaa	N	Y	2	H-bond	2, 3, 4
<b>SU-108</b>	2D	hcb	<i>P</i> 2 <sub>1</sub> / <i>n</i>	7	ZrO <sub>7</sub>	2aaba	N	Y	2	H-bond/π-π	1, 2, 3, 4
<b>SU-104</b>	2D	hcb	<i>P</i> -1	7	ZrO <sub>7</sub>	2aaaa	N	Y	2	H-bond	1, 2
<b>SU-111</b>	2D	hcb	<i>C</i> 2/ <i>c</i>	7	ZrO <sub>7</sub>	2aaaa	Y	Y	2	--	none
<b>SU-102</b>	3D	nbo	<i>R</i> -3 <i>c</i>	8	ZrO <sub>8</sub>	2baab	N	Y	1	H-bond	2, 3
<b>SU-103</b>	3D	pcu	<i>P</i> -1	7	Zr <sub>2</sub> O <sub>12</sub>	--	N	Y	2	H-bond	2, 4
<b>SU-105</b>	3D	dia	<i>C</i> 2/ <i>m</i>	8	ZrO <sub>8</sub>	1aaba	N	N	3	H-bond	1, 2
<b>SU-107</b>	3D	dia	<i>P</i> -1	7	ZrO <sub>7</sub>	1bbba	N	N	2	H-bond	2
<b>SU-109</b>	3D	dia	<i>P</i> -1	7	ZrO <sub>7</sub>	2baab	N	N	2	H-bond	2, 3
<b>SU-106</b>	3D	dia- <i>i</i>	<i>F</i> ddd	8	ZrO <sub>8</sub>	1abab	N	N	1	H-bond	1, 2, 4
<b>SU-112</b>	3D	dia- <i>i</i> 90°	<i>I</i> 4 <sub>1</sub> / <i>a</i> cd	8	ZrO <sub>8</sub>	1abab	N	N	1	H-bond	1, 2, 4

**dim.**, dimensionality; **C.N.**, coordination number; **ZrEA<sub>4</sub> isomer**, refers to the isomer codes defined in Supplementary Fig. 19-20; **Term. EA**, the presence (Y) or absence (N) of terminally coordinating non-bridging ellagate ligands; **EA π-π**, the presence (Y) or absence (N) of π-π interactions between ellagate linkers; **No. unique amines**, the number of crystallographically independent amines in the pores; **dia-*i***, an interpenetrated diamond net; **dia-*i*90°**, an interpenetrated diamond net with frameworks related by translation and a 90° rotation; **host-guest interactions**, excludes electrostatic and van der Waals interactions in this table as they are present in all reported structures; \* **H-bonding oxygen** specify which oxygen atoms on the ellagate linkers are involved as hydrogen-bond acceptors to the OSDAs, as defined later in Fig. 5a.

emphasized that each of these MOFs are indeed distinct phases as any one framework cannot be converted into another without breaking and/or forming new bonds. A summary of structural features is presented in Table 1. The differences in the structures become apparent upon inspection of the coordination environment around the Zr(IV) cations in each structure (Supplementary Fig. 13). The most obvious difference is the coordination number of the Zr(IV) cation. There is only one crystallographically unique Zr(IV) cation in each structure, to which four ellagate anions coordinate, forming a Zr(EA)<sub>4</sub> motif, except for SU-103 which is made of Zr<sub>2</sub>O<sub>12</sub> dimers. It should be noted that, in all but one of the MOFs, each ellagate bridges and is shared by two Zr(IV) cations and so the Zr:EA ratio is 1:2, except for SU-111 in which one of the four ellagate ligands is terminally coordinating resulting in a ratio of 1:2.5.

In four of the MOFs (SU-102, SU-105, SU-106, and SU-112), the Zr(IV) cation has a coordination number of eight (ZrO<sub>8</sub>) in a distorted square antiprism coordination geometry, with all four coordinating ellagate ligands chelating to Zr(IV) through both phenolic oxygen atoms of the catecholate group. However, in the other seven MOFs (SU-103, SU-104, SU-107, SU-108, SU-109, SU-110 and SU-111) the coordination number of Zr(IV) is seven (ZrO<sub>7</sub>) with coordination polyhedra that generally resemble distorted monocapped triangular prisms.

Close inspection of the Zr(EA)<sub>4</sub> coordination environment in the various MOFs reveals distinct differences between MOFs even with the same Zr(IV) coordination number and coordination polyhedron. The local structures of the various Zr(EA)<sub>4</sub> in MOFs with square antiprism ZrO<sub>8</sub> coordination polyhedra are compared in Fig. 3. Despite all having square antiprism coordination geometries, the orientations of the ellagate ligands differ, resulting in numerous distinct isomers of Zr(EA)<sub>4</sub>.

As an example, the frameworks of SU-102, SU-105 and SU-106 all with ZrO<sub>8</sub> square antiprism coordination polyhedra, are each composed of different Zr(EA)<sub>4</sub> isomers. To systemically classify and distinguish the isomers, we have considered two factors: 1) the pairing of the phenolic oxygen vertices around the ZrO<sub>8</sub> site, and 2) the orientations of the four ellagate ligands.

Firstly, each ellagate ligand chelates to the Zr(IV) centres through a catecholate group which contributes a pair of adjacent oxygen atoms to the ZrO<sub>8</sub> square antiprism coordination polyhedron. We have identified three possible combinations of such pairs to give eight vertices in a square antiprism (denoted as pairings 1, 2 and 3 in Fig. 3 and Supplementary Fig. 14-15). The coordination polyhedra become chiral when vertices are paired, and thus each complex has an enantiomeric opposite (denoted + and -), yet isomers of both handedness are present in each of the MOFs reported here as they crystallize in centrosymmetric space groups. Simplified representations of the ZrO<sub>8</sub> coordination environments are shown in the bottom two rows of Fig. 3. These representations clearly indicate how the oxygen vertices are paired (1, 2 or 3). SU-102 has oxygen pairing type 2, while SU-105, SU-106 and SU-112 all have a type 1 pairing.

Secondly, once the pairing of oxygen vertices has been established, the orientation of each ellagate ligand is considered. Each chelating ellagate ligand can have one of two orientations, related to one another by flipping the ligand to swap the positions of the two coordinating phenolic oxygen atoms of the catecholate. For clarity, the phenolic oxygen that is *meta* to the biaryl C-C bond is coloured blue in Fig. 3. The two orientations of EA are arbitrarily denoted *a* and *b* for each of the four

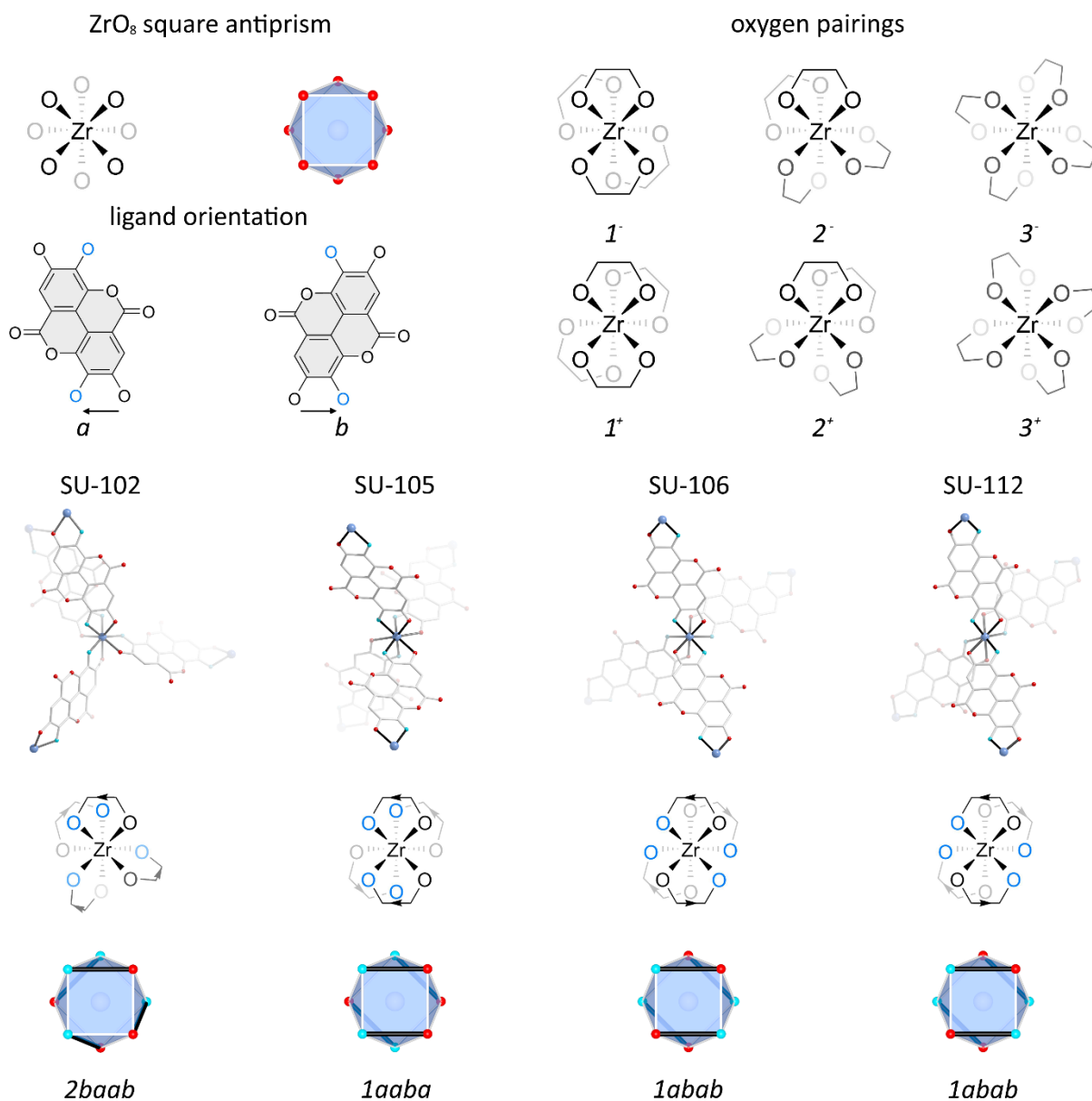


**Figure 3 | Zr(EA)<sub>4</sub> isomers for ZrO<sub>8</sub> square antiprisms found in the reported MOFs.** **ZrO<sub>8</sub> square antiprism**, Coordination environment of an ideal ZrO<sub>8</sub> square antiprism as a molecular sketch and polyhedral representation. **Oxygen pairings**, six ways to pair oxygen vertices in a square antiprism. **Ligand orientation**, Each ellagate ligand coordinating to Zr(IV) can have one of two orientations. One of the two phenolic oxygen atoms is coloured blue for clarity. **SU-1XX top**, Coordination environment around the 8-coordinated Zr(IV) cation in each MOF. **SU-1XX middle**, Simplified representations of the Zr(EA)<sub>4</sub> isomers. The two phenolic oxygen atoms of a single catecholate group are shown paired. Arrows indicate the orientation of the ellagate ligand. **SU-1XX bottom**, Further simplification of the Zr(EA)<sub>4</sub> isomers as idealized square antiprisms. Paired oxygen vertices are marked with a black line. The orientation of the ellagate ligand is indicated by the colours of the paired oxygen vertices in the direction from red to blue. The systematic code for the isomer is indicated on the bottom with the number (1, 2, or 3) indicating the specific pairing of oxygen vertices, followed by a sequence of four letters (a or b) indicating the specific orientations of the four ellagate ligands.

ellagate linkers (see Supplementary Fig. 16-17 for details). Fig. 3 shows that SU-105 and SU-106 have the same oxygen pairing, type 1, but are distinct from one another as the orientations of three of the four ellagate ligands are flipped, with SU-105 and SU-106 having the orientations *aaba* and *abab* respectively. On the other hand, SU-106 and SU-112 are built of the same Zr(EA)<sub>4</sub> isomer, *1abab*, however these MOFs are still regarded as distinct phases due to the aforementioned differences in framework interpenetration.

As the presented MOFs are composed of a variety of distinct Zr(EA)<sub>4</sub> isomers, we have attempted to classify those with ZrO<sub>8</sub> square antiprism and ZrO<sub>7</sub> monocapped triangular prism coordination geometries to systematically distinguish them from one another and to predict other possible isomers. Considering the ZrO<sub>8</sub> coordination environment with four ellagate

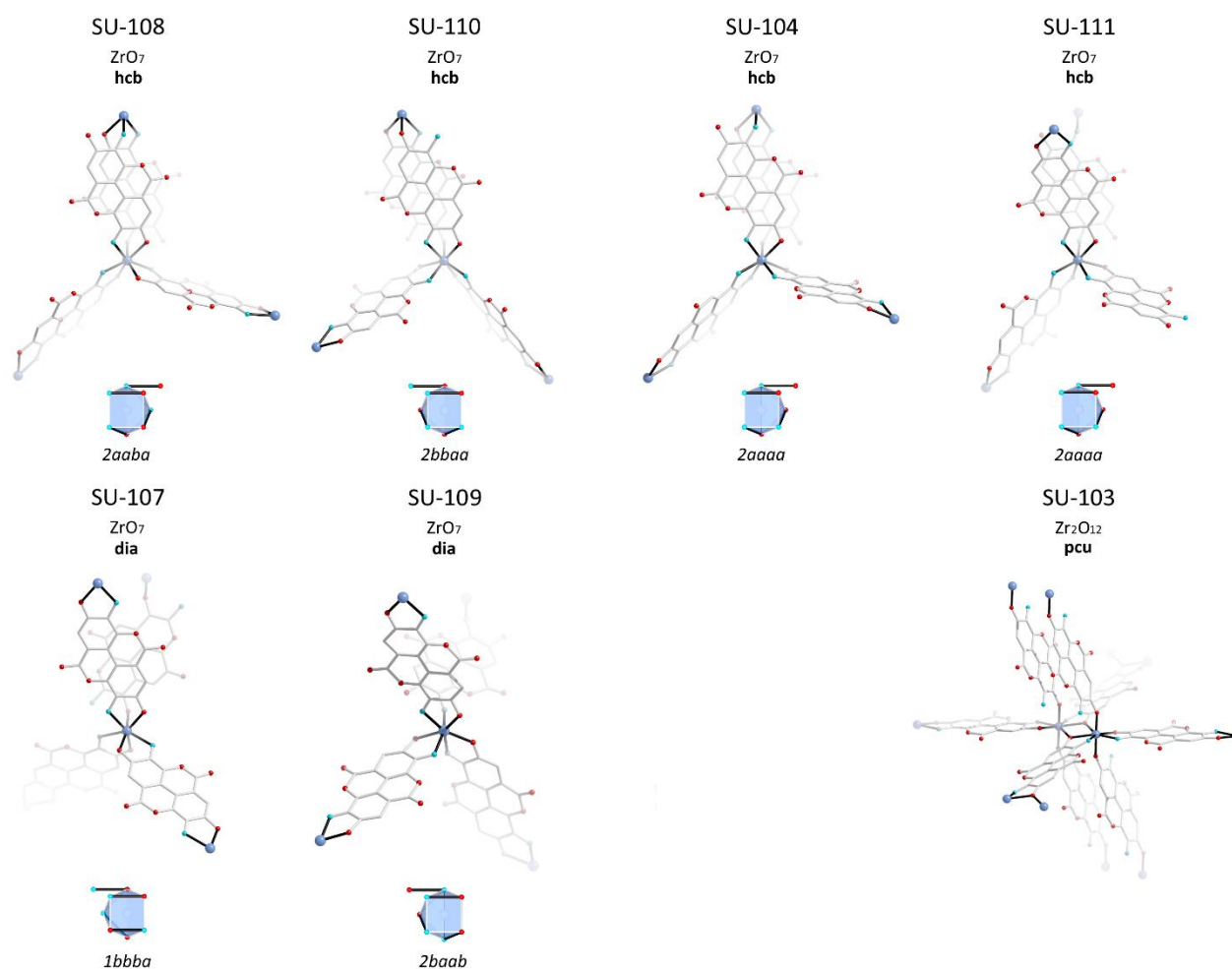


**Figure 4 | Local structures around Zr(EA)<sub>4</sub> for reported MOFs with 7-coordinated Zr(IV).** Simplified representations of the Zr(EA)<sub>4</sub> isomers are indicated below as well as the corresponding code according to Supplementary Fig. 20. SU-104 and SU-111 have the same isomers but the ellagate ligands connect to Zr(IV) cations in different ways. Unlike the other reported MOFs, SU-103 is made of dimeric Zr<sub>2</sub>O<sub>12</sub> units. One of the two phenolic oxygen atoms of each ellagate catechol is coloured blue to clarify the differences in ellagate orientations as described in Fig. 3.

ligands per Zr(IV) centre, each with two possible orientations, a total of 16 combinations of ellagate orientations are possible. With six different ways to pair oxygen vertices, each with 16 possible ellagate orientations, a total of 96 combinations were modelled. A simplified representation of these square antiprism isomers and all 96 combinations are presented in Supplementary Fig. 18-19. However, many of these are redundant as they are related by rotation. Considering this, we have identified 21 unique chiral pairs of isomers of Zr(EA)<sub>4</sub> square antiprisms, resulting in a total of 42 isomers. It should be noted that all the synthesized MOFs are centrosymmetric and thus each structure consists of both enantiomers. However, only three of these 21 isomer pairs have been observed in the reported MOFs so far. As such, the three isomers described herein are, while possibly energetically favourable, just scratching the surface in terms of structural diversity in this system.

For Zr(EA)<sub>4</sub> with the Zr(IV) in a ZrO<sub>7</sub> environment, the coordination polyhedra mostly resemble a distorted monocapped triangular prism, although exceptions such as SU-107 and SU-109 more closely resemble distorted pentagonal bipyramids. There are four ways the oxygen vertices are paired (1<sup>+</sup>, 1<sup>-</sup>, 2<sup>+</sup> and 2<sup>-</sup>), each with 16 possible ellagate orientations (xxxx where each x can be a or b), resulting in a total of 64 possible chiral isomers or 32 enantiomeric pairs (Supplementary Fig. 20). Of these 32, only five have been observed so far amongst the reported MOFs (2aaaa, 2aaba, 1bbba, 2bbaa, 2baab) as illustrated in Fig. 4.

We also anticipate the possibility of Zr<sub>2</sub>O<sub>12</sub> isomers of Zr<sub>2</sub>(EA)<sub>8</sub> by flipping the orientations of the ellagate linkers, although these have not yet been considered in this study.

## OSDA-framework interactions

The ammonium-based OSDAs with a various chemical properties (Supplementary Table 4) form different types of intermolecular interactions with the host MOF frameworks. All OSDAs are charge-balancing cations that have coulombic (electrostatic) interactions with the anionic frameworks where the anionic sites are deprotonated phenolate oxygen atoms. In all as-synthesized MOF structures except SU-111, the OSDAs are hydrogen-bond donors and interact with the frameworks through hydrogen bonds between the nitrogen atoms of ammonium sites and various hydrogen-bond accepting oxygen atoms of the ellagate ligands. In one ellagic acid molecule, there are two phenol oxygen atoms from catechol groups located at both the *para* (**1**) and *meta* (**2**) positions of the biaryl C-C bond, as well as two different types of oxygen atoms in lactones, an ether (**3**) and a carbonyl (**4**) oxygen. These four different types of oxygen atoms are marked with their numerical codes in Fig. 5a. The various OSDAs form hydrogen bonds to different ellagate oxygen atoms in the MOFs. As hydrogen atoms are difficult to locate directly from experimental 3D ED data, we interpret donor-acceptor distances  $\leq 3.3$  Å as hydrogen bonds.

The interaction with different oxygen atoms results in varied distributions of the OSDAs in the various MOFs. The specific oxygen types that form hydrogen bonds in each structure are summarised in Table 1. It can be seen that oxygen atom type **2** (i.e. the phenol oxygen atom *meta* to the biaryl C-C bond) is the most common site for hydrogen bonding, with at least one OSDA in ten of the eleven zirconium ellagate structures (SU-102 – SU-112) interacting with this particular oxygen site. The only exception is SU-111 formed from tetramethylammonium which is not a hydrogen-bond donor. Hydrogen bonds formed with the phenol oxygen **1** or the carbonyl oxygen **4** are both observed in five of the MOFs, while the ether oxygen **3** is less frequently involved in hydrogen bonding, appearing in only four structures. As an example, Fig. 5b and 5c shows the locations of the two unique OSDAs in SU-103 and their interactions with ellagate ligands. The nitrogen atom shown in Fig. 5b is located at the edge of the pore, forming hydrogen bonds with type **2** phenol oxygen atoms from two ligands. A second OSDA (Fig. 5c) is positioned between two ligands, forming hydrogen bonds with the carbonyl oxygen atoms of two ligands.

In addition to hydrogen-bonding interactions,  $\pi$ - $\pi$  stacking involving the OSDAs also contributes to the stabilization of the obtained materials. These interactions primarily occur when OSDAs with benzene rings were used, such 4-*tert*-butylaniline in SU-108, and can be observed between the OSDA and the framework, but also between adjacent OSDA molecules. The two crystallographically unique 4-*tert*-butylanilinium found in SU-108 are packed by T-shaped  $\pi$ - $\pi$  stacking. One of the OSDAs only forms hydrogen bonds with the framework while the second OSDA interacts with the framework by  $\pi$ - $\pi$  stacking as shown in Fig. 5d. Although the *tert*-butyl group at the tail of the molecule requires more space and causes the OSDA and the ligand to not completely align, the shortest distance between the benzene ring plane of the OSDA and the ligand plane is 3.6 Å, indicating the presence of  $\pi$ - $\pi$  stacking.

The assembly of the OSDA molecules in the pores of the MOF frameworks play a crucial role in structure-direction and can be understood by concepts of steric templating effects and space filling. Three general interactions can be identified: (1) The metal node and its connected ligands create pocket of space at the corners of the pores where OSDAs snugly fit in. (2) OSDAs occupy the space between layers, supporting and stabilizing the layered structure. (3) OSDAs stretch along the channels and cavities of the framework, filling the pores. There can be more than one type of arrangement as two or three crystallographically unique OSDAs can exist in a single structure. Crystal structures of all MOFs with OSDA are shown in Supplementary Fig. 21.

For structures formed by smaller amines with short alkyl chains or small cyclic structures, such as in SU-102, SU-107, SU-108 and SU-111, the OSDAs tend to fit into pockets formed at the junctions between the metal and ligands. Apart from tetramethylammonium in SU-111, these are more peripheral amines with a higher degree of polarization and seemingly tend to form 3D frameworks where the nitrogen atom of the ammonium cation occupies the corners of the pore windows<sup>31</sup>. In the structure of SU-107, the small size of the DABCO cations allow them to perfectly occupy pocket sites at the corners of the larger pore (Fig. 5e). In SU-108, in which two crystallographically unique OSDAs are present, one of the amines fits in the corners of the pores, while another one occupies the interlayer space. A similar mechanism can be observed in SU-104 and SU-110, where hindered and bulky tertiary ammonium cations with long carbon chains of six or eight carbon atoms, respectively, yield layered structures. As shown in Fig. 5f, two of the carbon chains from one OSDA in SU-104 align parallel to the layers, occupying the interlayer voids and stabilizing the layered structure. The third chain, however, tends to extend into the pore. For SU-109 with the shorter alkyl chains in tributylammonium the resulting MOF is instead a 3D framework.

In the remaining structures, OSDAs mainly occupy the pore space and guide the formation of the framework around them. For the MOFs made from secondary ammonium species such as SU-103 and SU-105, as previously discussed, the *n*-butyl or *i*-butyl alkyl chains of the secondary ammonium species extend through the channels or cages resulting in 3D frameworks.

Primary diammonium cations appears to be a special case, resulting in the interpenetrated framework structures of SU-106 and SU-112. In SU-112 (Fig. 5h), the two individual frameworks are linked by methylpentamethylenediammonium through hydrogen bonds, and it appears as though ammonium sites on opposite ends of a sufficiently long molecule promotes the generation of an interpenetrated structure.

In summary, the OSDAs with cyclic structures or shorter alkyl chains are more likely to stabilize in pockets at the corners of the pores. In contrast, the OSDAs with long chain groups tend to have a space-filling role and steric effects are dominant. When OSDAs bearing long carbon chains are used (more than five aliphatic carbons per side chain), layered structures are obtained as the OSDA partially fills the pores as well as the interlayer space. In addition, MOFs with interpenetrated structures appear to be obtained when diamines are used as OSDAs.

During the synthesis of the described MOFs, the Zr(IV) and ellagcate ligands likely organize around the OSDA, directing the MOF structure based on its size, shape and host-guest interactions. As such, hydrogen bonding and  $\pi$ - $\pi$  stacking likely play significant roles in the assembly of specific structures in addition to electrostatic and van der Waals interactions. Considering this diversity of interactions, the role of OSDAs in this Zr-ellagcate system is rather different than that observed in templated inorganic porous materials, owing to the presence of both inorganic and organic species in the MOF materials.

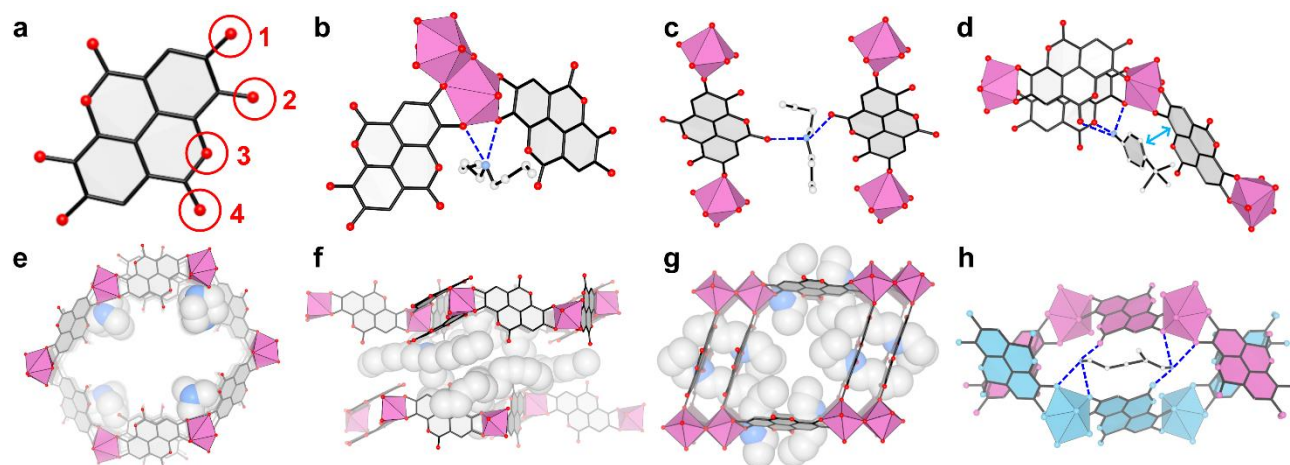


**Figure 5 | Host-guest interactions between OSDAs and the zirconium-ellagcate frameworks.** **a**, Ellagic acid with the four different types of oxygen atoms labelled. **b,c**, Hydrogen bonds between dibutylammonium and the framework in SU-103. Hydrogen bonds are marked as dashed blue lines. **d**, Hydrogen bonds and  $\pi$ - $\pi$  stacking interactions between 4-*tert*-butylanilinium and the framework in SU-108.  $\pi$ - $\pi$  stacking is marked in light blue arrows. **e-g**, Crystal structures of SU-107, SU-104 and SU-103, respectively. The OSDAs are shown as space-filling models. **h**, Interactions between 2-methylpentamethylenediammonium and the framework in SU-112. The two interpenetrating frameworks are colored pink and blue.

## Ion exchange

To verify the stability of the MOFs and free up the pore space within the open anionic Zr(IV)-ellagcate frameworks, ion exchange experiments were carried out to replace the cationic OSDAs with smaller monovalent metal cations such as  $\text{Na}^+$  and  $\text{K}^+$ . Ion exchange was performed for 24 h at room temperature in aqueous salt solutions. All MOFs indicated stability as confirmed by PXRD, with the exception of SU-112 which underwent amorphization (Supplementary Fig. 30). The PXRD patterns of SU-107 after  $\text{Na}^+$  and  $\text{K}^+$  ion exchange exhibited large peak shifts indicating significant structural changes likely due to framework dynamics.

Energy dispersive X-ray spectroscopy (EDS) indicated a M:Zr ratio of 1:1 (where  $\text{M} = \text{Na}^+$  or  $\text{K}^+$ ) for MOFs including SU-103 and SU-105 (see Supplementary Table 3), whereas SU-107 and SU-102 showed a M:Zr ratio closer to 2:1. It is noteworthy that in the case of SU-104, SU-109 and SU-110, ion exchange was incomplete as indicated by very low M:Zr ratio, which is attributed to the more hydrophobic character of the trialkylammonium OSDAs (trihexylammonium, tributylammonium, and trioctylammonium respectively). In an attempt to promote a higher degree of ion exchange, these experiments were repeated for SU-104, SU-109 and SU-110 at  $80^\circ\text{C}$  instead. Only SU-109, with trialkylammonium as the OSDA and the shortest alkyl chains amongst the tertiary ammonium cations, showed an increase in the M:Zr ratio at higher temperatures which approached 2:1 (Supplementary Table 3). Higher temperatures or the use of less polar solvents or cations may be required to promote ion exchange to replace the more hydrophobic OSDAs such as trihexylammonium or trioctylammonium. Noticeably, the crystals of SU-104, SU-109 and SU-110 exhibited distinctly hydrophobic behavior<sup>32</sup> during ion exchange attempts compared to the other MOFs. Only these hydrophobic crystals floated to the top of the aqueous salt solution when stirred and problematically stuck to the upper walls of the glass vials above the level of the solution. It appears as the hydrophobicity of the ammonium cations is translated to the MOF crystals. PXRD indicates that hydrophobic SU-104, SU-109 and SU-110 were highly stable and largely unaffected by the attempted ion exchange experiments.

## Stability of the zirconium-ellagate frameworks

The stability of the zirconium-ellagates SU-103 – SU-112 under various conditions such as in water at 80 °C, hydrothermal conditions at 180 °C, acidic and basic media (pH 1, 2, 11, 12, 13), organic solvents (DMF, THF, chlorobenzene, toluene, hexane, methanol, acetonitrile and acetone), aqueous 1M NaCl and KCl solutions, and elevated temperatures in air was investigated by PXRD (Supplementary Fig. 23-30) and thermogravimetric analysis (TGA, Supplementary Fig. 31). A summary is provided in Table 2.

The MOFs generally demonstrated stability under basic conditions as all MOFs were stable at a pH of at least 11 or higher with SU-112 being the least stable, while SU-103, SU-105, and SU-108 were robust even at a pH of 13. Acid stability was more varied as some MOFs had degraded at a pH of 2 (SU-105, SU-106, SU-109 and SU-112), while others demonstrated even higher stability than SU-102 at a pH of 1 (SU-103, SU-104, SU-108 and SU-110). The MOFs also were stable in the selected organic solvents. It should be noted however that for the layered structure SU-110 with the most hydrophobic OSDA, trioctylammonium, peaks in the PXRD pattern remained but were severely broadened when exposed to nonpolar solvents (hexane, THF and toluene). Most MOFs were also stable in 1M NaCl and 1M KCl solution with the exceptions of SU-107 and SU-112, although it should be noted that the MOFs with more hydrophobic OSDAs including SU-104, SU-109 and SU-110 with trialkylammonium OSDAs only showed very limited ion exchange. All MOFs are stable to water at room temperature, while only SU-112 degrades at 80 °C, and SU-103, SU-104 and SU-108 were fully stable under hydrothermal conditions at 180 °C.

Overall metal-ellagate MOFs do not exhibit particularly high thermal stability in air compared to many other MOFs, since ellagic acid, notorious as an antioxidant, easily oxidises. TGA experiments provide further evidence for the hydrophobic characters of SU-104, SU-109 and SU-110. Unlike the other MOFs made from more hydrophilic OSDAs, the TGA curves of SU-104, SU-109 and SU-110 lack a small step around 35-110 °C commonly associated with loss of water from the pores. Interestingly, the PXRD pattern of SU-107 drastically changes upon heating suggesting rather significant framework dynamics between room temperature and 40°C. This indicates that while most of the other MOFs are rather rigid, SU-107 is noticeably dynamic and flexible.

When comparing stability (Table 2) with structural features of the MOFs (Table 1), it appears as if MOFs with  $\pi$ - $\pi$  stacking between ellagate linkers have higher general stability (SU-102, SU-103, SU-104, SU-108, SU-110), while the dimensionality of the MOFs (3D frameworks vs 2D layers) or the Zr(IV) coordination number (7 or 8) are less influential towards stability.

**Table 2 | Stability of zirconium-ellagate frameworks.** Values in the tables indicate conditions in which the MOFs are still stable.

	H <sub>2</sub> O	Base /pH	Acid /pH	1M NaCl and KCl	Organic solvents <sup>1</sup>	Air
<b>SU-102</b> <sup>2</sup>	180°C	13	2	Stable	Stable	300°C
<b>SU-103</b>	180°C	13	1	Stable	Stable	250°C
<b>SU-104</b>	180°C	12	1	Stable	Stable	200°C
<b>SU-105</b>	80°C	13	>2	Stable	Stable	200°C
<b>SU-107</b>	80°C	12	>2	Unstable	Stable	40°C, 100°C <sup>3</sup>
<b>SU-108</b>	180°C	13	1	Stable	Stable	150°C
<b>SU-109</b>	180°C <sup>4</sup>	12	>2	Stable	Stable	200°C
<b>SU-110</b>	80°C	12	1	Stable	Partial <sup>5</sup>	150°C
<b>SU-112</b>	RT	11	>2	Unstable	Stable	200°C

<sup>1</sup>Organic solvents investigated include DMF, THF, chlorobenzene, toluene, hexane, methanol, acetonitrile and acetone. <sup>2</sup>As previously reported<sup>17</sup>. <sup>3</sup>PXRD shows significant changes at 40°C indicating structure dynamics followed by loss of crystallinity at 150°C. <sup>4</sup>Partial conversion to SU-102. <sup>5</sup>PXRD peaks remain after organic solvent stability test but are severely broadened.

## Conclusions

Ten anionic pseudo-polymorphic Zr(IV)-ellagate MOFs were synthesized using ten different amines as organic structure-directing agents (OSDAs) under otherwise identical reaction conditions. Each MOF has a unique structural profile with one of various possible topologies, inorganic building units, Zr(IV) coordination numbers, intermolecular framework interactions, pore size, and dimensionality. These structural differences, as well as the differences in the chemical properties of the OSDAs, resulted in different physical and chemical properties of the MOFs such as hydrophobicity/hydrophilicity, and rigid or dynamic frameworks. In particular,  $\pi$ - $\pi$  interactions within the frameworks appear to govern the stability of these MOFs.

By further changing the species of the OSDA, we envision that a plethora of other MOFs could potentially be synthesized within this zirconium ellagate system alone, considering the predicted possibility of numerous other 7- and 8-coordinated Zr(EA)<sub>4</sub> isomers that are yet to be observed. Other potential SDAs may include other amines or ammonium species that have not yet been used in this study, as well as various organic cations such as phosphonium or sulfonium species, or even cationic metal complexes.

While ion exchange to replace the ammonium species for monovalent metal cations was performed in this study, ion exchange with other organic cations could lead to further tuning of the accessible pore volume, as well as of the nature of the interior surface of the material, or for introducing functional groups that may be of interest for chemical reactions within the MOF pores.

## Methods

All chemicals were used as-received without further purification. The reagents were obtained as follows: reagent-grade ellagic acid (97% H<sub>4</sub>EA) was purchased from BLD Pharmatech Ltd., zirconyl chloride octahydrate (98% ZrOCl<sub>2</sub>·8H<sub>2</sub>O) was purchased from Honeywell, glacial acetic acid (100% AcOH) was purchased from Merck.

### Synthesis of SU-102

Synthesis of SU-102 was modified from a previously reported procedure<sup>17</sup>. ZrOCl<sub>2</sub>·8H<sub>2</sub>O (32 mg, 0.1 mmol), ellagic acid (60 mg, 0.2 mmol), deionized water (2.5 mL), acetic acid (1.0 mL) and N,N-dimethylformamide (DMF, 1.0 mL) were combined in a borosilicate 3.3 glass tube (Duran 12 × 100 mm, DWK Life Sciences). The glass tube was then sealed with a polybutylene terephthalate (PBT) cap containing a PTFE seal and heated at 160 °C in an aluminium heating block for 1 h while stirring. After cooling the glass tube to room temperature, the resulting brown suspension was then centrifuged at 10,000 rpm for 10 minutes and decanted. The remaining yellow solid was then dried overnight at 80 °C.

### Synthesis of SU-103

ZrOCl<sub>2</sub>·8H<sub>2</sub>O (32 mg, 0.1 mmol), ellagic acid (60 mg, 0.2 mmol), deionized water (2.5 mL), acetic acid (1.0 mL) and N,N-dibutylformamide (DBF, 1.0 mL) were combined in a borosilicate 3.3 glass tube (Duran 12 × 100 mm, DWK Life Sciences). The glass tube was then sealed with a PBT cap containing a PTFE seal and heated at 160 °C in an aluminium heating block for 1 h while stirring. After cooling the glass tube to room temperature, the resulting brown suspension was then centrifuged at 10,000 rpm for 10 minutes and decanted. The remaining brown solid was then dried overnight at 80 °C.

### Synthesis of SU-104

ZrOCl<sub>2</sub>·8H<sub>2</sub>O (32 mg, 0.1 mmol), ellagic acid (60 mg, 0.2 mmol), deionized water (2.5 mL), acetic acid (1.0 mL) and trihexylamine (THA, 1.0 mL) were combined in a borosilicate 3.3 glass tube (Duran 12 × 100 mm, DWK Life Sciences). The glass tube was then sealed with a PBT cap containing a PTFE seal and heated at 160 °C in an aluminium heating block for 1 h while stirring. After cooling the glass tube to room temperature, the resulting brown suspension was then centrifuged at 10,000 rpm for 10 minutes and decanted. The remaining brown solid was then dried overnight at 80 °C.

### Synthesis of SU-105

ZrOCl<sub>2</sub>·8H<sub>2</sub>O (32 mg, 0.1 mmol), ellagic acid (60 mg, 0.2 mmol), deionized water (2.5 mL), acetic acid (1.0 mL) and diisobutylamine (DIBA, 1.0 mL) were combined in a borosilicate 3.3 glass tube (Duran 12 × 100 mm, DWK Life Sciences). The glass tube was then sealed with a PBT cap containing a PTFE seal and heated at 160 °C in an aluminium heating block for 1 h while stirring. After cooling the glass tube to room temperature, the resulting brown suspension was then centrifuged at 10,000 rpm for 10 minutes and decanted. The remaining brown solid was then dried overnight at 80 °C.

### Synthesis of SU-106

ZrOCl<sub>2</sub>·8H<sub>2</sub>O (32 mg, 0.1 mmol), ellagic acid (60 mg, 0.2 mmol), deionized water (2.5 mL), acetic acid (1.0 mL) and hexane-1,6-diamine (HDA, 1.0 mL) were combined in a borosilicate 3.3 glass tube (Duran 12 × 100 mm, DWK Life Sciences). The glass tube was then sealed with a PBT cap containing a PTFE seal and heated at 160 °C in an aluminium heating block for 1 h while stirring. After cooling the glass tube to room temperature, the resulting brown suspension was then centrifuged at 10,000 rpm for 10 minutes and decanted. The remaining brown solid was then dried overnight at 80 °C.

### Synthesis of SU-107

To obtain SU-107 the reagents were added in the following order; ZrOCl<sub>2</sub>·8H<sub>2</sub>O (32 mg, 0.1 mmol), ellagic acid (60 mg, 0.2 mmol), deionized water (2.5 mL), acetic acid (1.0 mL) and then 1,4-diazabicyclo[2.2.2]octane (DABCO, 1.0 g) in a borosilicate 3.3 glass tube (Duran 12 × 100 mm, DWK Life Sciences). The glass tube was then sealed with a PBT cap containing a PTFE seal and heated at 160 °C in an aluminium heating block for 1 h while stirring. After cooling the glass tube to room temperature, the resulting brown suspension was then centrifuged at 10,000 rpm for 10 minutes and decanted. The remaining brown solid was then dried overnight at 80 °C.

### Synthesis of SU-108

ZrOCl<sub>2</sub>·8H<sub>2</sub>O (32 mg, 0.1 mmol), ellagic acid (60 mg, 0.2 mmol), deionized water (2.5 mL), acetic acid (1.0 mL) and 4-*tert*-butylaniline (4TBA, 1.0 ml) were combined in a borosilicate 3.3 glass tube (Duran 12 × 100 mm, DWK Life Sciences). The glass tube was then sealed with a PBT cap containing a PTFE seal and heated at 160 °C in an aluminium heating block for 1 h while stirring. After cooling the glass tube to room temperature, the resulting brown suspension was then centrifuged at 10,000 rpm for 10 minutes and decanted. The remaining brown solid was then dried overnight at 80 °C.

#### Synthesis of SU-109

ZrOCl<sub>2</sub>·8H<sub>2</sub>O (32 mg, 0.1 mmol), ellagic acid (60 mg, 0.2 mmol), deionized water (2.5 mL), acetic acid (1.0 mL) and tributylamine (TBA, 1.0 ml) were combined in a borosilicate 3.3 glass tube (Duran 12 × 100 mm, DWK Life Sciences). The glass tube was then sealed with a PBT cap containing a PTFE seal and heated at 160 °C in an aluminium heating block for 1 h while stirring. After cooling the glass tube to room temperature, the resulting brown suspension was then centrifuged at 10,000 rpm for 10 minutes and decanted. The remaining brown solid was then dried overnight at 80 °C.

#### Synthesis of SU-110

ZrOCl<sub>2</sub>·8H<sub>2</sub>O (32 mg, 0.2 mmol), ellagic acid (60 mg, 0.2 mmol), deionized water (2.5 mL), acetic acid (1.0 mL) and trioctylamine (TOA, 1.0 ml) were combined in a borosilicate 3.3 glass tube (Duran 12 × 100 mm, DWK Life Sciences). The glass tube was then sealed with a PBT cap containing a PTFE seal and heated at 160 °C in an aluminium heating block for 1 h while stirring. After cooling the glass tube to room temperature, the resulting brown suspension was filtered and washed with 50 mL of deionized water. The remaining brown solid was then dried overnight at 80 °C.

#### Synthesis of SU-111

ZrOCl<sub>2</sub>·8H<sub>2</sub>O (32 mg, 0.1 mmol), ellagic acid (60 mg, 0.2 mmol), deionized water (2.5 mL), acetic acid (1.0 mL) and tetramethylammonium hydroxide (35% wt. in H<sub>2</sub>O) (TMAOH, 1.0 ml) were combined in a borosilicate 3.3 glass tube (Duran 12 × 100 mm, DWK Life Sciences). The glass tube was then sealed with a PBT cap containing a PTFE seal and heated at 160 °C in an aluminium heating block for 1 h while stirring. After cooling the glass tube to room temperature, the resulting brown suspension was then centrifuged at 10,000 rpm for 10 minutes and decanted. The remaining brown solid was then dried overnight at 80 °C.

#### Synthesis of SU-112 (MPDA)

ZrOCl<sub>2</sub>·8H<sub>2</sub>O (32 mg, 0.1 mmol), ellagic acid (60 mg, 0.2 mmol), deionized water (2.5 mL), acetic acid (1.0 mL) and 2-methylpentamethylenediamine (MPDA, 1.0 mL) were combined in a borosilicate 3.3 glass tube (Duran 12 × 100 mm, DWK Life Sciences). The glass tube was then sealed with a PBT cap containing a PTFE seal and heated at 160 °C in an aluminium heating block for 1 h while stirring. After cooling the glass tube to room temperature, the resulting brown suspension was then centrifuged at 10,000 rpm for 10 minutes and decanted. The remaining brown solid was then dried overnight at 80 °C. PXRD indicated a phase mixture with SU-102.

#### Synthesis of SU-112 (DABCO)

As an alternative synthesis procedure to obtain SU-112, MPDA was replaced by DABCO. Reagents were added in the following order; ZrOCl<sub>2</sub>·8H<sub>2</sub>O (32 mg, 0.1 mmol), ellagic acid (60 mg, 0.2 mmol), deionized water (2.5 mL), 1,4-diazabicyclo[2.2.2]octane (DABCO, 1.0 g) and then acetic acid (1.0 mL) in a borosilicate 3.3 glass tube (Duran 12 × 100 mm, DWK Life Sciences). The glass tube was then sealed with a PBT cap containing a PTFE seal and heated at 160 °C in an aluminium heating block for 1 h while stirring. After cooling the glass tube to room temperature, the resulting brown suspension was filtered and washed with 50 mL of deionized water. The remaining brown solid was then dried overnight at 80 °C. This procedure with DABCO formed phase pure SU-112 which was used for characterization.

#### Acid and base stability

10 mg of the corresponding MOF was immersed in 1 mL of each respective solvent or solution, which was added to the same glass-tubes used for synthesizing the material. The tubes were then sealed with PBT caps containing a PTFE seal and were subsequently stirred and heated to various temperatures for 24 h. Solutions of various pH were prepared by adding NaOH or HCl to deionized water in order to obtain the desired pH (Supplementary Fig. 22-30).

#### Ion exchange

100 mg of the as-synthesized SU-MOF was ion-exchanged by stirring the MOF in 6 mL 1M NaCl or KCl solution for 24 hours at room temperature. For the more hydrophobic MOFs synthesized with trialkylamines, ion exchange was also performed at 80 °C. The ion-exchanged MOF was separated by centrifugation at 3800 rpm for 10 minutes and the process was repeated a second time. After washing, the ion-exchanged MOF was dried in an oven at 70 °C overnight (Supplementary Fig. 22-30).

#### General characterization

In-house powder X ray diffraction (PXRD) measurements were carried out using a Panalytical X'pert Pro diffractometer (Cu K $\alpha_{1,2}$ ,  $\lambda_1 = 1.540598 \text{ \AA}$ ,  $\lambda_2 = 1.544426 \text{ \AA}$ ) using a Bragg-Brentano geometry (Supplementary Fig. 22-30). Variable-temperature PXRD measurements were carried out using a Bruker D8 Discover diffractometer, equipped with an Anton Paar XRK 900 reaction chamber (Supplementary Fig. 22-30). Thermogravimetric analysis (TGA) data (Supplementary Fig. 31) of as-synthesized MOFs were collected using a Perkin Elmer TGA 7. SU-106 and SU-111 were not fully characterized for stability tests nor was ion exchange performed as these phases were obtained as phase mixtures.

#### Three-dimensional electron diffraction and topological analysis

Three-dimensional electron diffraction (3D ED) data (Supplementary Tables 1–2) were collected using a JEOL JEM2100 TEM, equipped with a Timepix detector from Amsterdam Scientific Instruments, while continuously rotating the crystal at 0.45° s<sup>-1</sup>. The experiment was carried out using Instamatic<sup>33</sup>, with data reduction performed in XDS<sup>34</sup>. The acquired intensities were then used to solve the structures with SHELXT<sup>35</sup>, and refined using SHELXL<sup>36</sup> using electron scattering factors and interfaced with Olex2-1.5<sup>37</sup>. From the 3D ED data, all non-hydrogen atoms of the frameworks were located in the initial structure solution. In most cases all non-hydrogen atoms of the ammonium species were also located in the initial structure solution. For ammonium species with long flexible alkyl chains, some of the more disordered peripheral atoms were geometrically placed in chemically reasonable positions and their positions were refined while applying distance and angle restraints. Topological analysis was carried out using the software package ToposPro<sup>38</sup>.

## Scanning transmission electron microscopy

High-resolution scanning transmission electron microscope (STEM) imaging was performed using a Thermo Fisher Themis Z operated at an accelerating voltage of 300 kV. A Cs-aberration corrector ensured optimal probe coherence by correcting aberrations up to the fifth order prior to image acquisition. The monochromator facilitated a reduction in the probe beam current to approximately 1 pA (Fluscreen reading). A four-segment annular dark-field (ADF) detector collected scattered electrons within an angular range of 6–34 mrad. The illumination geometry employed a conical probe with a semi-convergence angle of 10 mrad at a camera length of 230 mm. Image reconstruction for optimum bright-field (OBF)-STEM was achieved using in-house developed code based on methods described elsewhere<sup>39,40</sup>. A nonlinear filter was utilized on OBF-STEM images for denoising<sup>41</sup>. The lattice-averaged potential maps were obtained by crystallographic image processing using the software CRISP<sup>44,42</sup>.

## Acknowledgements

E.S.G. and A.K.I. acknowledge support from the Swedish Foundation for Strategic Research (SSF). A.K.I. and A.L.-O. acknowledge support from the Wallenberg Initiative Materials Science for Sustainability (WISE) funded by the Knut and Alice Wallenberg Foundation. A.L.-O. acknowledges support from SECTEI (SECTEI/142/2023). E.S.G. acknowledges support from the Swedish Research Council (grant no. 2022-06178). T.W. and Y.Z. acknowledge support from Formas – a Swedish Research Council for Sustainable Development (2022-01270). T.W. and Y.X. acknowledge support from the Carl Trygger Foundation (CTS 20:471). The authors thank Miguel Rivero Crespo for insightful discussions.

## Author contributions

E.S.G. designed, synthesized, and, by 3D ED, solved the crystal structures of SU-103 – SU-111 and contributed to the conceptualization of the study. T.W. and A.K.I. contributed to the conceptualization and supervision of the study. A.L.-O. synthesized and characterized SU-103 – SU-112. Y.X. performed STEM imaging. Y.Z. collected 3D ED data and refined the crystal structures of SU-103 – SU-112. All authors contributed to the writing of the manuscript.

## Competing financial interests

The authors declare no competing financial interests.

## References

1. Barrer, R. M. Zeolites and their synthesis. *Zeolites* **1**, 130–140 (1981).
2. Moliner, M., Rey, F. & Corma, A. Towards the rational design of efficient organic structure-directing agents for zeolite synthesis. *Angew. Chemie Int. Ed.* **52**, 13880–13889 (2013).
3. Fang, Q. *et al.* Amine-templated assembly of metal–organic frameworks with attractive topologies. *Cryst. Growth Des.* **8**, 319–329 (2008).
4. Zhao, N. *et al.* Organic amines as templates: pore imprints with exactly matching sizes in a series of metal–organic frameworks. *Chem. Commun.* **54**, 11264–11267 (2018).
5. Zhang, Z. & Zaworotko, M. J. Template-directed synthesis of metal–organic materials. *Chem. Soc. Rev.* **43**, 5444–5455 (2014).
6. Ghosh, S. K. & Kitagawa, S. Solvent as structure directing agent for the synthesis of novel coordination frameworks using a tripodal flexible ligand. *CrystEngComm* **10**, 1739–1742 (2008).
7. Panda, T., Pachfule, P. & Banerjee, R. Template induced structural isomerism and enhancement of porosity in manganese(II) based metal-organic frameworks (Mn-MOFs). *Chem. Commun.* **47**, 7674–7676 (2011).
8. Zhao, N., Cai, K. & He, H. The synthesis of metal-organic frameworks with template strategies. *Dalt. Trans.* **49**, 11467–11479 (2020).
9. Liu, Y., Kravtsov, V. C., Larsen, R. & Eddaoudi, M. Molecular building blocks approach to the assembly of zeolite-like metal–organic frameworks (ZMOFs) with extra-large cavities. *Chem. Commun.* 1488–1490 (2006).
10. Yuan, S., Qin, J. S., Lollar, C. T. & Zhou, H. C. Stable Metal-Organic Frameworks with Group 4 Metals: Current Status and Trends. *ACS Cent. Sci.* **4**, 440–450 (2018).
11. Fan, W. *et al.* Aluminum metal–organic frameworks: From structures to applications. *Coord. Chem. Rev.* **489**, 215175 (2023).
12. Mouchaham, G. *et al.* A Robust Infinite Zirconium Phenolate Building Unit to Enhance the Chemical Stability of Zr MOFs. *Angew. Chemie - Int. Ed.* **54**, 13297–13301 (2015).
13. Mouchaham, G. *et al.* Adaptability of the metal(III,IV) 1,2,3-trioxobenzene rod secondary building unit for the production of chemically stable and catalytically active MOFs. *Chem. Commun.* **53**, 7661–7664 (2017).
14. Chen, E. X. *et al.* Acid and Base Resistant Zirconium Polyphenolate-Metalloporphyrin Scaffolds for Efficient CO<sub>2</sub> Photoreduction. *Adv. Mater.* **30**, 1–8 (2018).
15. Feng, X. *et al.* Elucidating J-Aggregation Effect in Boosting Singlet-Oxygen Evolution Using Zirconium-Porphyrin Frameworks: A Comprehensive Structural, Catalytic, and Spectroscopic Study. *ACS Appl. Mater. Interfaces* **11**, 45118–45125 (2019).

16. Grape, E. S. *et al.* A robust and biocompatible bismuth ellagate MOF synthesized under green ambient conditions. *J. Am. Chem. Soc.* **142**, 16795–16804 (2020).
17. Svensson Grape, E. *et al.* Removal of pharmaceutical pollutants from effluent by a plant-based metal–organic framework. *Nat. Water* **1**, 433–442 (2023).
18. Liu, T.-B. *et al.* Stable calcium ellagate metal–organic frameworks as high-performance green memorizers bearing high working temperatures. *Inorg. Chem. Front.* **11**, 3056–3062 (2024).
19. Chai, R. *et al.* Superior Oxygen Evolution Electrocatalyst based on Ni-Ellagic Acid Coordination Polymer. *Adv. Energy Mater.* 2400871.
20. Lin, W. *et al.* Efficient Photocatalytic CO<sub>2</sub> Reduction in Ellagic Acid–Based Covalent Organic Frameworks. *J. Am. Chem. Soc.* (2024).
21. Zhang, Z. *et al.* Efficient adsorption of acetylene over CO<sub>2</sub> in bioinspired covalent organic frameworks. *J. Am. Chem. Soc.* **144**, 14992–14996 (2022).
22. Gemmi, M. *et al.* 3D electron diffraction: The nanocrystallography revolution. *ACS Cent. Sci.* **5**, 1315–1329 (2019).
23. Huang, Z., Svensson Grape, E., Li, J., Inge, A. K. & Zou, X. 3D electron diffraction as an important technique for structure elucidation of metal-organic frameworks and covalent organic frameworks. *Coord. Chem. Rev.* **427**, 213583 (2021).
24. Huang, Z., Willhammar, T. & Zou, X. Three-dimensional electron diffraction for porous crystalline materials: structural determination and beyond. *Chem. Sci.* **12**, 1206–1219 (2021).
25. Luo, Y. *et al.* High-throughput phase elucidation of polycrystalline materials using serial rotation electron diffraction. *Nat. Chem.* **15**, 483–490 (2023).
26. Wang, B. *et al.* A Porous Cobalt Tetraphosphonate Metal–Organic Framework: Accurate Structure and Guest Molecule Location Determined by Continuous-Rotation Electron Diffraction. *Chem. - A Eur. J.* **24**, 17429–17433 (2018).
27. Ge, M., Yang, T., Xu, H., Zou, X. & Huang, Z. Direct Location of Organic Molecules in Framework Materials by Three-Dimensional Electron Diffraction. *J. Am. Chem. Soc.* **144**, 15165–15174 (2022).
28. Svensson Grape, E., Rooth, V., Nero, M., Willhammar, T. & Inge, A. K. Structure of the active pharmaceutical ingredient bismuth subsalicylate. *Nat. Commun.* **13**, 1–7 (2022).
29. Korde, A. *et al.* Single-walled zeolitic nanotubes. *Science* **375**, 62–66 (2022).
30. Delgado Friedrichs, O., O’Keeffe, M. & Yaghi, O. M. Three-periodic nets and tilings: regular and quasiregular nets. *Acta Crystallogr. Sect. A Found. Crystallogr.* **59**, 22–27 (2003).
31. Dolui, D., Mir, A. Q. & Dutta, A. Probing the peripheral role of amines in photo- And electrocatalytic H<sub>2</sub> production by molecular cobalt complexes. *Chem. Commun.* **56**, 14841–14844 (2020).
32. Xie, L. H., Xu, M. M., Liu, X. M., Zhao, M. J. & Li, J. R. Hydrophobic Metal–Organic Frameworks: Assessment, Construction, and Diverse Applications. *Adv. Sci.* **7**, (2020).
33. Cichocka, M. O., Ångström, J., Wang, B., Zou, X. & Smeets, S. High-throughput continuous rotation electron diffraction data acquisition via software automation. *J. Appl. Crystallogr.* **51**, 1652–1661 (2018).
34. Kabsch, W. XDS. *Acta Crystallogr. Sect. D Biol. Crystallogr.* **66**, 125–132 (2010).
35. Sheldrick, G. M. SHELXT - Integrated space-group and crystal-structure determination. *Acta Crystallogr. Sect. A Found. Crystallogr.* **71**, 3–8 (2015).
36. Sheldrick, G. M. A short history of SHELX. *Acta Crystallogr. Sect. A Found. Crystallogr.* **64**, 112–122 (2008).
37. Dolomanov, O. V., Bourhis, L. J., Gildea, R. J., Howard, J. A. K. & Puschmann, H. OLEX2: A complete structure solution, refinement and analysis program. *J. Appl. Crystallogr.* **42**, 339–341 (2009).
38. Blatov, V. A., Shevchenko, A. P. & Proserpio, D. M. Applied Topological Analysis of Crystal Structures with the Program Package ToposPro. *Cryst. Growth Des.* **14**, 3576–3586 (2014).
39. Seki, T. *et al.* Quantitative electric field mapping in thin specimens using a segmented detector: Revisiting the transfer function for differential phase contrast. *Ultramicroscopy* **182**, 258–263 (2017).
40. Ooe, K. *et al.* Direct imaging of local atomic structures in zeolite using optimum bright-field scanning transmission electron microscopy. *Sci. Adv.* **9**, eadf6865 (2023).
41. Du, H. A nonlinear filtering algorithm for denoising HR (S) TEM micrographs. *Ultramicroscopy* **151**, 62–67 (2015).
42. Hovmöller, S. CRISP: crystallographic image processing on a personal computer. *Ultramicroscopy* **41**, 121–135 (1992).